Nano Energy 34 (2017) 15–25

Contents lists available at ScienceDirect

Nano Energy

journal homepage: www.elsevier.com/locate/nanoen

Full paper

# Superior performance of ordered macroporous $TiNb_2O_7$ anodes for lithium ion batteries: Understanding from the structural and pseudocapacitive insights on achieving high rate capability

Shuaifeng Lou[a,b], Xinqun Cheng[a], Yang Zhao[b], Andrew Lushington[b], Jinlong Gao[a], Qin Li[a], Pengjian Zuo[a], Biqiong Wang[b], Yunzhi Gao[a], Yulin Ma[a], Chunyu Du[a], Geping Yin[a,*], Xueliang Sun[b,*]

[a] MIIT Key Laboratory of Critical Materials Technology for New Energy Conversion and Storage, School of Chemistry and Chemical Engineering, Harbin Institute of Technology, Harbin 150001, China
[b] Department of Mechanical and Materials Engineering, University of Western Ontario, London, ON, Canada N6A 5B9

ARTICLE INFO

*Keywords:*
Lithium ion batteries
Hierarchical nanostructure
Single-crystalline nanoparticles
Pseudocapacitive behavior
Rate capability

ABSTRACT

Titanium niobium oxide ($TiNb_2O_7$) has been regarded as a promising anode material for high-rate lithium ion batteries (LIBs) due to its potential to operate at high rates with improved safety and high theoretical capacity of 387 mA h $g^{-1}$. Herein, three-dimensionally ordered macroporous (3DOM) $TiNb_2O_7$ composed of interconnected single-crystalline nanoparticles was prepared using polystyrene (PS) colloidal crystals as a hard template. The final product yields a homogeneous, continuous, and effective honeycomb-like construction. This architecture provides facile $Li^+$ insertion/extraction and fast electron transfer pathway, enabling high-performance lithium ion pseudocapacitive behavior, leading to good electrochemical performance. As a result, the 3DOM-$TiNb_2O_7$ shows a remarkable rate capability (120 mA h $g^{-1}$ at 50 C) and durable long-term cyclability (82% capacity retention over 1000 cycles at 10 C). The work presented herein holds great promise for future design of material structure, and demonstrates the great potential of $TiNb_2O_7$ as a practical high-rate anode material for LIBs.

## 1. Introduction

Lithium ion batteries (LIBs) have become ubiquitous power sources for portable electronics by virtue of their high energy density and power density. The potential application of these energy storage devices in pure electric vehicles (EVs), hybrid electric vehicles (HEVs), and large-scale energy storage have been demonstrated [1–4]. Graphite is widely used as the anode material in commercial LIBs, but it cannot satisfy the increasing demand required for high power application. As an alternative to commercial graphite anode in high-rates LIBs, spinel $Li_4Ti_5O_{12}$ has been extensively investigated because it exhibits excellent lithium ion insertion/extraction reversibility with “zero strain” at a relatively higher operating voltage (1.55 V vs. $Li^+$/Li), ensuring long cycle life and additional safety by avoiding lithium dendrite formation [5,6]. Despite these obvious advantages, the specific capacity of $Li_4Ti_5O_{12}$ is only 175 mA h $g^{-1}$, a fraction of the energy density provided by graphite (372 mA h $g^{-1}$). As a consequence, the practical application in the full batteries of $Li_4Ti_5O_{12}$ anode is limited due to its relatively low energy density.

In 2011, $TiNb_2O_7$ was proposed by Goodenough's group as a high rate anode material, demonstrating potential to replace $Li_4Ti_5O_{12}$ [7,8]. Subsequently, it attracted much research interest because of its outstanding electrochemical performance [9–12]. The theoretical capacity of $TiNb_2O_7$ is 387.6 mA h $g^{-1}$ corresponding to a 5-electron transfer reaction ($Ti^{4+}/Ti^{3+}$, $Nb^{5+}/Nb^{3+}$), which is almost two times higher than that of $Li_4Ti_5O_{12}$ [13]. Meanwhile, the high voltage plateau of $TiNb_2O_7$ (~1.64 V) can avoid the formation an SEI layer, resulting in a rapid $Li^+$ intercalation/deintercalation and longer cycle life compared to carbon-based electrodes [14]. In addition, the slow rise/drop characteristic near the end of the charge/discharge process observed in the voltage-time curve is conductive to the precise estimation for state of charge (SOC), which is typically based on a predetermined OCV–SOC relationship (OCV: open-circuit voltage) [14]. This is especially important for the development of battery pack management systems used in EV [15]. In contrast, $Li_4Ti_5O_{12}$ generally shows a very flat voltage plateau followed by an abrupt rise/drop following the charge/discharge

* Corresponding author.
*E-mail addresses:* yingeping@hit.edu.cn (G. Yin), xsun@eng.uwo.ca (X. Sun).

http://dx.doi.org/10.1016/j.nanoen.2017.01.058
Received 6 November 2016; Received in revised form 30 January 2017; Accepted 31 January 2017
Available online 01 February 2017

process, leading to difficulty in estimating SOC. This information is especially difficult to ascertain when combined with a cathode material exhibiting similar charge/discharge characteristics, such as the $LiFePO_4$ cathode. For these reasons, the $TiNb_2O_7$ exhibits enormous potential to replace $Li_4Ti_5O_{12}$ as the next generation anode material for high-power lithium ion batteries.

However, the intrinsic low electronic and ionic conductivity of $TiNb_2O_7$ have restricted its electrochemical kinetics [16]. To address these problems, several efforts have already been completed to improve the electrochemical properties [17–19]. Thereinto, synthesis of nanoscale electrode materials [20–24] has proved to be an effective approach since nanometer size particles can dramatically reduce $Li^+$ ion diffusion time and improve $Li^+$ insertion/extraction kinetics by shortening the $Li^+$ solid diffusion pathway. Beyond that, reduced particle size of dozens of nanometers has been shown to produce significant pseudocapacitive effects [25]. Take into consideration that pseudocapacitive charge storage is not a diffusion-controlled process and can significantly enhance the rate performance and reversibility in lithium-ion batteries [26]. Previous work by Dunn et al. demonstrates great promise towards high-rate electrodes in LIBs driven by an intercalation pseudocapacitive mechanism [27]. However, nanosized insertion-type anode materials typically suffer from poor crystal structure stability and low tap density, reducing the cycling stability and volumetric energy density that can be obtained. Hence a tradeoff occurs between high-rate performance and cycling stability. It is challenging, but desirable, to enhance the electrochemical performance of a host material without sacrificing stability. One simple and effective way to alleviate this issue is to prepare micro-scale materials with hierarchically nanostructured configuration, merging advantages of fast $Li^+$ transport and structure stability together.

Three-dimensionally ordered macroporous (3DOM) structure, with an interconnected network of nanometer thick walls, is an attractive architecture for electrode materials. 3DOM materials provide an intercontinuous network of pores for ample contact with liquid electrolyte. Meanwhile, the continuous walls provide three-dimensional transport pathways for electron and lithium ion conduction [28], improving electronic and ionic conductivity. Typically, the 3DOM structure is obtained by replicating the structure of a colloidal crystal template stacked by microspheres [29,30]. Hence, it presents a high surface-area-to-volume ratio with nanometer sized walls for short diffusion lengths and a high active surface area for a large number of intercalation sites [28], More than that, the hierarchical nanostructure can also be conducive to the intercalation pseudocapacitive behavior. Up to now, the construction and the performance of 3DOM structured $TiNb_2O_7$ anode materials have not been reported.

Herein, the 3DOM-$TiNb_2O_7$ was first prepared and used as an anode material for high-rate lithium ion batteries. The obtained 3DOM structure presents a hierarchical architecture and is composed of interconnected single-crystalline nanoparticles in the nanometer range. The 3DOM-$TiNb_2O_7$ exhibits an average reversible capacity of 135 mA h $g^{-1}$ at a charge rate of 20 C, even delivers high reversible capacities of 120 and 99 mA h $g^{-1}$ at charge rates of 50 C and 100 C, respectively. Furthermore, this presented material can maintain a capacity retention ratio of 82.3% following 1000 cycles at 10 C. Furthermore, given the unique architecture of 3DOM-$TiNb_2O_7$ demonstrated that intercalation pseudocapacitance dominates the fast charge storage process in the 3DOM-$TiNb_2O_7$ anodes and strongly contributes to the superior rate capability and long cycle life of LIBs.

## 2. Experimental section

### 2.1. Preparation of 3DOM-$TiNb_2O_7$

Monodispersed polystyrene (PS) dispersions were synthesized using emulsifier-free emulsion polymerization technology. The PS spheres were close-packed into colloidal crystals by drying at 50 °C for 24 h. These dried samples were used as hard templates in the synthesis of three-dimensionally ordered macroporous $TiNb_2O_7$. Precursor solutions were obtained by dissolving a desired amount of mixed metal salt [$NbCl_5$/$C_{16}H_{36}O_4Ti$=2/1, mol] into absolute ethyl alcohol solvent at room temperature. Subsequently, the PS colloidal crystals were soaked in precursor solution for 12 h. Excess solution was removed from the impregnated PS template by vacuum filtration. The obtained sample was dried in air at 50 °C for 24 h. The polystyrene spheres were removed by calcination in air atmosphere at 900 °C for 5 h at a heating rate of 1 °C $min^{-1}$.

### 2.2. Materials characterization

Size and morphology of 3DOM-$TiNb_2O_7$ was characterized using a Helios Nanolab 600i high-resolution Field Emission Scanning Electron Microscope (FESEM) operating at 10 kV. Transmission electron microscopy (TEM) and high resolution TEM (HRTEM) images were taken with a TecnaiG2F30 transmission electron microscope with an acceleration voltage of 300 kV. The crystal structure of the samples was confirmed by X-ray powder diffraction (XRD) carried out on a Rigaku D/max-γA X-ray diffractometer with Cuκα radiation (λ=1.54178 Å). The $N_2$ adsorption/desorption isotherms of the samples were performed at 77 K using 3H-2000PS2 (Beishide Instrument Technology Co., Ltd), and the specific surface area was calculated from the BET plot of the $N_2$ adsorption isotherm. To investigate the valence bond of $TiNb_2O_7$, a Raman spectrometer (Horiba Jobin Yvon, LabRam Aramis) and the FT-IR spectrometer (ThermoNicolet iS10) with an attenuated total reflectance (ATR) unit were used to obtain the Raman and FT-IR spectrum. The X-ray photoelectron spectra (XPS) was recorded on a PHI 5700 ESCA system fitted with Al κα radiation.

### 2.3. Electrochemical performance measurements

The electrochemical performance of the $TiNb_2O_7$ sample was analyzed in $TiNb_2O_7$/Li half cells. The working electrodes were fabricated as follows. First, the 3DOM-$TiNb_2O_7$ (70 wt%), Super P (20 wt%), and polyvinylidene fluoride (PVDF 10 wt%) were mixed and then stirred in appropriate amount of N-methyl-2-pyrrolidone (NMP) to form a homogeneous black slurry. The black slurry was spread onto Cu foil via doctor blading. The electrode was dried in vacuum at 120 °C for 12 h and then punched into disks with diameter of 14 mm. The average loading weight of the active material in the coin cell fabrication is ~1.5 mg. Lithium metal was used as the counter electrode in the coin cell, and a porous polypropylene membrane (Celgard 2500) was used as the separator. CR2025-type coin cells were assembled in an argon-filled glove box with both moisture and oxygen contents below 0.5 ppm. The electrolyte was 1 mol $L^{-1}$ $LiPF_6$ in ethylene carbonate/dimethyl carbonate (EC/DMC, 1/1 by volume) solvent. The galvanostatic charge/discharge test (1.0–3.0 V) was performed on the Neware-CT3008 test system.

## 3. Results and discussion

As shown in Scheme 1, the 3DOM-$TiNb_2O_7$ was prepared by a facile hard template method. The close-packed PS colloidal crystals, utilized as a typical hard template, were soaked in precursor solution and the penetrant process proceed spontaneously through a capillary attraction for 12 h, while excess solution was removed by vacuum filtration along with an in situ hydrolysed process, followed by calcination in air to remove the PS hard template. SEM images of the monodispersed PS spheres and the self-assembly PS colloidal crystals are shown in Fig. S1. Fig. S1a shows uniform monodispersed PS spheres with the average diameter of ~325 nm. Fig. S1b, c and d give typical surface morphologies of the PS colloidal crystals array with a hexagonal closed-packed arrangement of PS particles. The interstices among the PS microspheres in Fig. S1d are the formation location of $TiNb_2O_7$ triangle

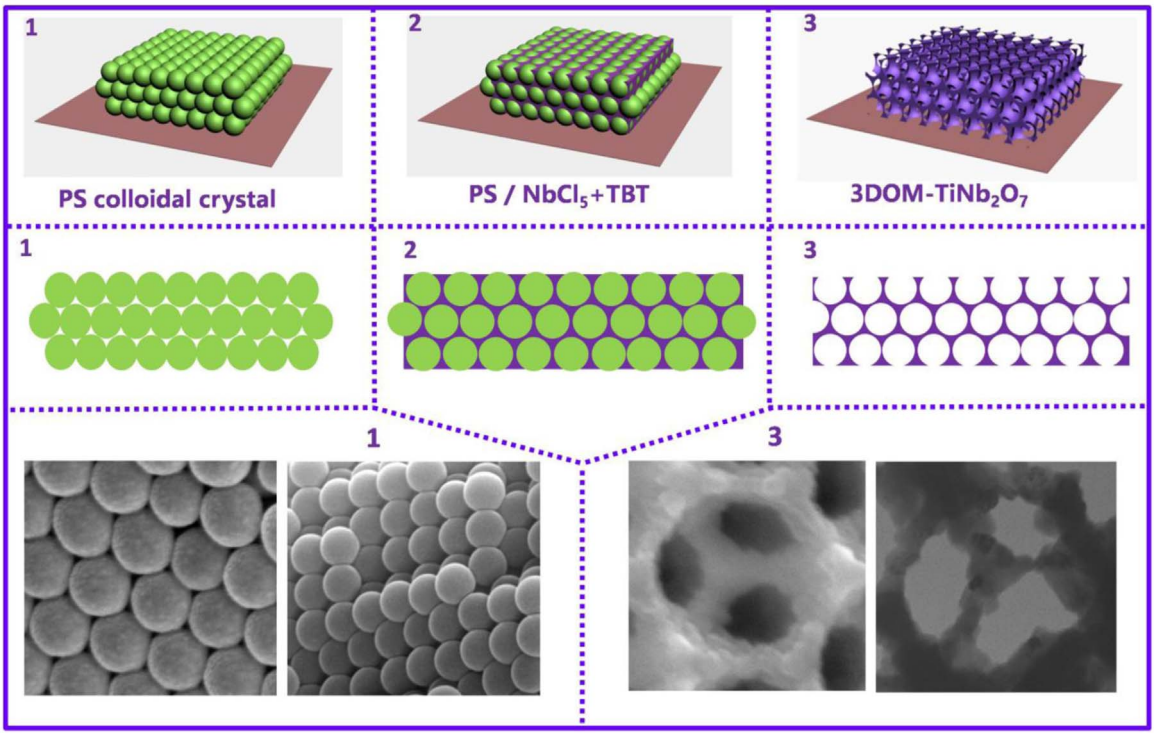


**Scheme 1.** Schematic illustration for preparation of 3DOM-$TiNb_2O_7$ anode materials using PS microspheres as a hard template.

array, as shown in the corresponding SEM and TEM images of a 3DOM-$TiNb_2O_7$ triangle array in Scheme 1.

Crystal structure of as-synthesized $TiNb_2O_7$ was confirmed by X-ray diffraction (XRD) analysis (Fig. 1a). All observed diffraction peaks are in good agreement with the standard XRD pattern (JCPDS: #77-1374), indicating good crystallinity of $TiNb_2O_7$. The characteristic diffraction peaks of (002), (110), (003) and (−602) can be assigned to '$ReO_3$' structure and belong to a monoclinic system (space group C2/m) with the lattice constants a=20.351 Å, b=3.801 Å, c=11.882 Å, and b=120.191 [31]. The Fig. 1a inset shows the crystal structure of the monoclinic $TiNb_2O_7$ phase along the *a*-axis. The $MO_6$ (M=Ti, Nb) octahedra present an 'A-B-A' layer structure, which can accommodate embedded $Li^+$ and maintain structure stability [13,16]. To further confirm the formation of $TiNb_2O_7$, FT-IR spectroscopy was used to

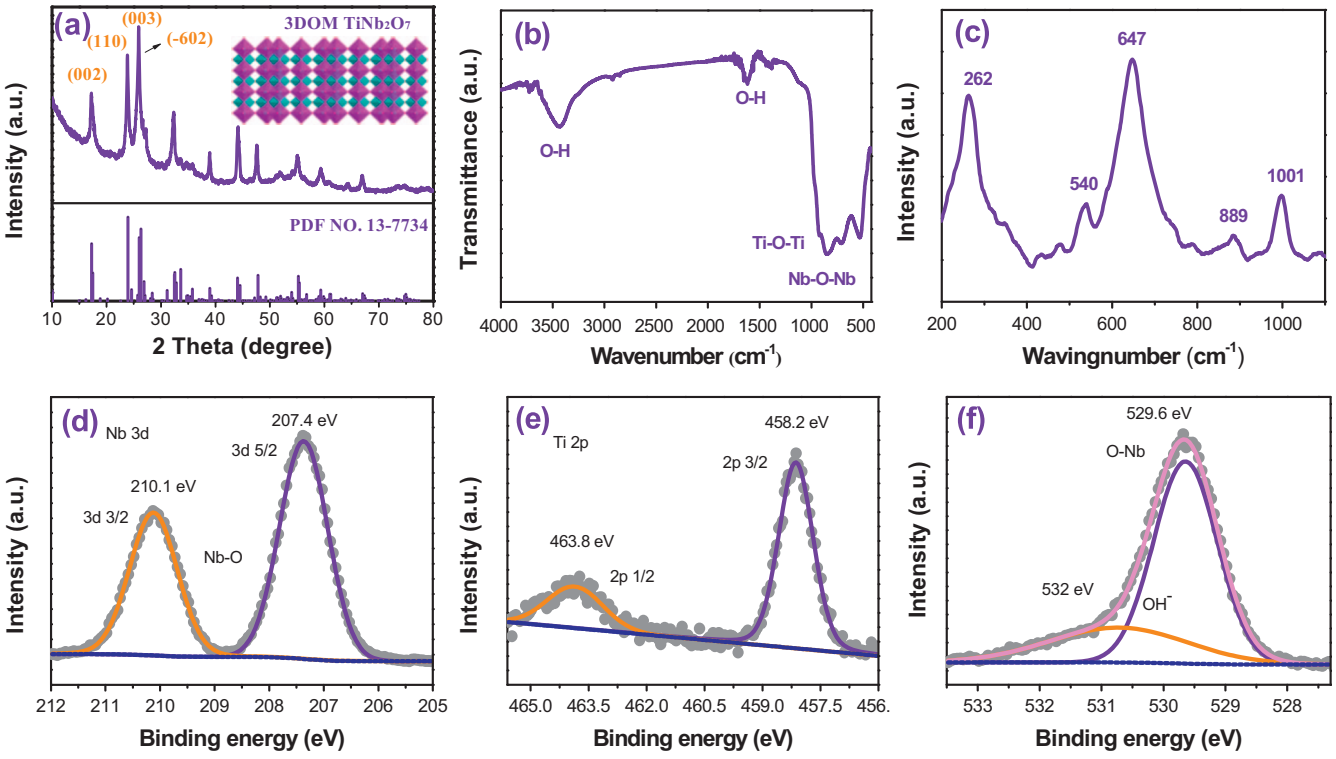


**Fig. 1.** (a) XRD pattern and standard pattern. (Inset) crystal structure of the monoclinic $TiNb_2O_7$ viewed along the *a*-axis. (b) FTIR spectra, (c) Raman spectroscopy, and high resolution XPS spectra for (d) Nb, (e) Ti and (f) O elements of the 3DOM -$TiNb_2O_7$.

reveal the bonding characteristics. As shown in Fig. 1b, the bonds at approximate 1650 $cm^{-1}$ and 3450 $cm^{-1}$ are attributed to the stretching vibrations of hydroxyl groups from the absorbed water vapour on the surface of $TiNb_2O_7$ [32]. The bands at 924 $cm^{-1}$ and 530 $cm^{-1}$ can be assigned to the stretching vibrations of the Nb-O bonds and the Nb-O-Nb bridging bonds, respectively. Finally, bands at 694 $cm^{-1}$ and 839 $cm^{-1}$ arise from stretching vibration of Ti-O-Ti bonds [33]. Structure of the monoclinic $TiNb_2O_7$ phase was also investigated by Raman spectroscopy, as shown in Fig. 1c. The two bands at 889 and 1001 $cm^{-1}$ can be assigned to symmetric metal–oxygen stretching vibrations of corner/edge-shared $NbO_6$ octahedra, respectively. The metal-oxygen vibrations of the $TiO_6$ octahedra occur at 540 and 647 $cm^{-1}$, while the band at 262 $cm^{-1}$ can be attributed to symmetric and antisymmetric bending vibrations of O–Ti–O, O–Nb–O [34]. Therefore, based on the above analysis, $TiNb_2O_7$ phase can be confirmed to be present following the thermal annealing process.

X-ray photoemission spectroscopy (XPS) was further employed to analyze the valence state information of Nb, Ti and O elements in $TiNb_2O_7$, as shown in Fig. S2. The broad spectrum obtained reveals the existence of Nb, Ti, O and C elements in the sample. The presence of C can be attributed to adsorbed carbon from the atmosphere [35]. Fig. 1d shows the HRXPS spectra of Nb, reveling a Nb 3d 5/2 peak is located at approximately 207.4 eV corresponding to $Nb^{5+}$, in good agreement with the binding energies in $Nb_2O_5$ [36], indicating that all of the Nb in $TiNb_2O_7$ is pentavalent. The XPS spectrum of Ti 2p double peak is presented in Fig. 1e and displays energies at about 463.8 eV and 458.2 eV, correspond to Ti 2p 1/2 and Ti 2p 3/2, respectively. The splitting data of 5.6 eV in core levels indicates a normal state of $Ti^{4+}$ in the oxide [17,37]. The main peak of O 1 s (Fig. 1f) is centered at 529.6 eV, which is attributed to oxygen species in the $TiNb_2O_7$ phase [17]. Another small peak at 531.1 eV can be ascribed to hydroxyl oxygen, which is also observed in FTIR data.

The morphology and microstructure of $TiNb_2O_7$ was observed using scanning electron microscopy (SEM) and transmission electron microscopy (TEM). Fig. 2a and Fig. S3 show the typical morphology of prepared 3DOM-$TiNb_2O_7$. It is observed that nearly all the obtained $TiNb_2O_7$ microparticles present three-dimensionally ordered porous structure. Fig. 2b shows a representative 3DOM structure, where the well-ordered “air spheres” and the interconnected inorganic walls create three-dimensional “honeycomb” pore structure [38,39]. Naturally, the open and interconnected 3DOM structure could give a high specific area to expose more surface sites. Fig. 2c shows a typical “honeycomb pore” structure unit with an average wall thickness of 50 nm and interconnected pore diameter of 100 nm. Fig. 2d and e presents the TEM images of obtained 3DOM-$TiNb_2O_7$ sample from different visual angles. Interestingly, the close packing arrangement of the original PS template (Fig. S1b-d) is successfully preserved after removing the PS template, highlighting the efficacy of our proposed synthesis route. Obviously, the dark regions correspond to the $TiNb_2O_7$ framework and the light regions correspond to the void space. Fig. 2d shows an ordered macroporous arrangement with a diameter of about 325 nm, corresponding to the results of the SEM images. It can be found in Fig. 2e that the well-ordered inorganic walls connected the ‘air spheres’ spread throughout the porous particle from different viewing direction compared with Fig. 2d. A clear connecting type can be observed in Fig. 2f, presenting a typical three dimensional ordered interconnected structure of $TiNb_2O_7$, well coinciding with the Scheme 1.

In order to further understand the architecture of the 3DOM-$TiNb_2O_7$, high resolution transmission electron microscopy (HRTEM) was performed to study the construction and crystalline phase. As shown in Fig. 3a, the typical “honeycomb” crosslinking structure consists of a rough inorganic wall with a diameter of about 50 nm and presents obvious regularity. Fig. 3b shows the enlarged area of the yellow box in Fig. 3a. It is observed that the interconnected walls are composed of nano-crystalline grains that are tightly linked together with a size of 20–40 nm. Fig. 3c shows an enlarged area of Fig. 3b, and presents several crystalline grains with different orientation existing in the selected region. The regular spacing of the lattice fringes of nano-crystallites is 0.34 nm, which is consistent with an interplanar distance

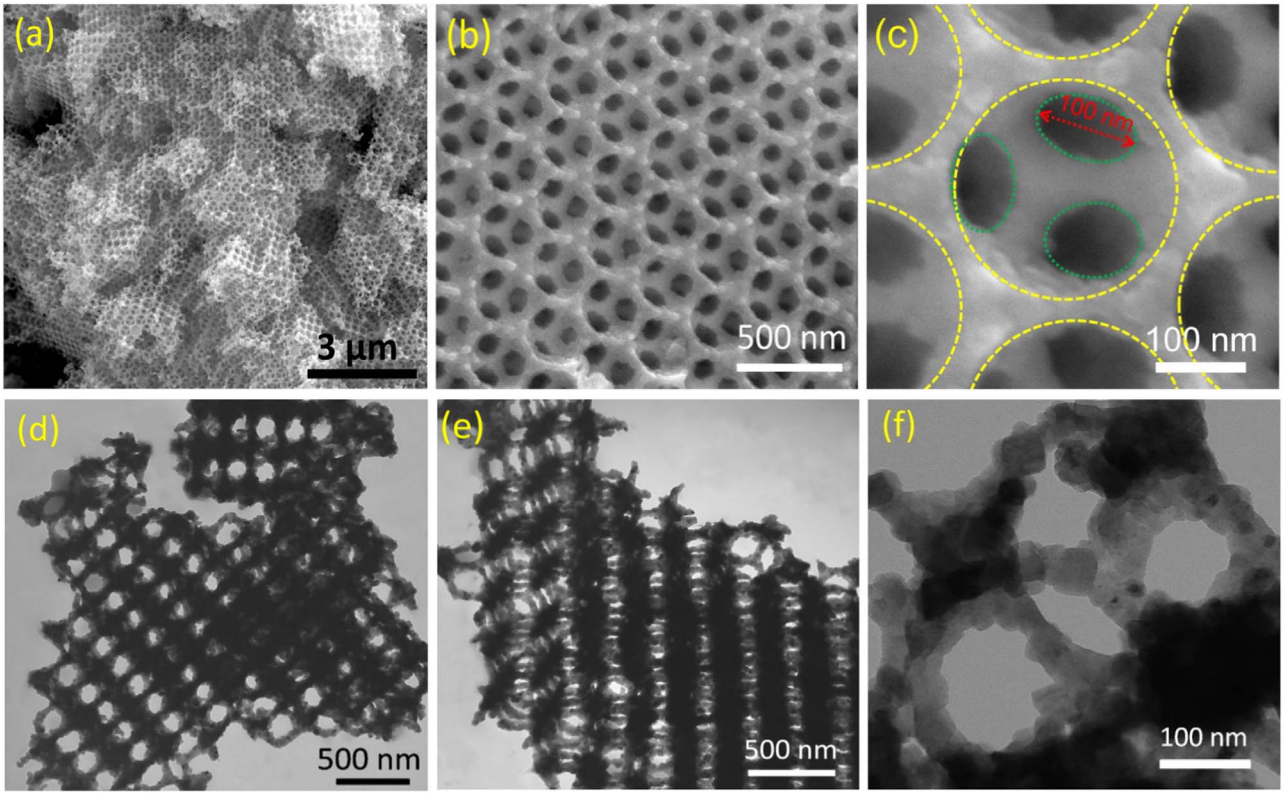


**Fig. 2.** SEM images (a, b, c) and TEM images (d, e, f) of the 3DOM $TiNb_2O_7$ after calcination at 900 °C for 5 h.

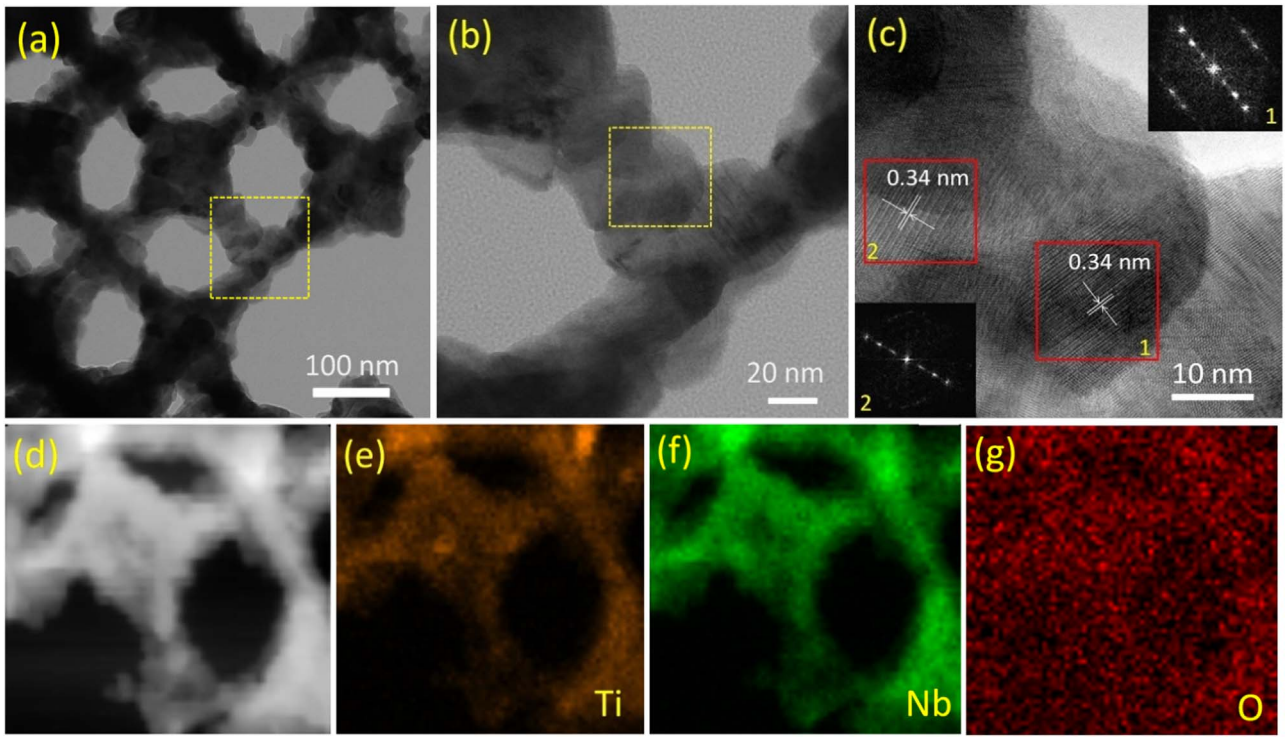


**Fig. 3.** (a) HRTEM image of the 3DOM-$TiNb_2O_7$ after calcination at 900 °C. (b) HRTEM image of the interconnected walls (enlarged image of the yellow box in Fig. 5a). (c) The lattice fringes of different crystalline grains (enlarged image of the yellow box in Fig. 4c), and the FFT results corresponding to the selected red box. (d) HAADF-STEM image of a pore unit in the 3DOM architecture. (e-g) Element mappings of the pore unit in the Fig. 3d.

of the (003) plane of $TiNb_2O_7$ [40]. A fast Fourier transform (FFT) of region 1 in Fig. 3c displays very sharp diffraction spot arrangements, revealing the single crystalline nature of the selected crystalline grain [41]. A similar phenomenon is also observed in the FFT result of region 2, suggesting a special oriented feature of $TiNb_2O_7$ crystal structure, which has been investigated in detail in our previous work [40]. Meanwhile, selected area electron diffraction (SAED) of a larger area was performed. The scattered diffraction points in Fig. S4 further confirm that the interconnected walls are composed of multiple single-crystalline nanoparticles. A similar 1D hierarchical structure named "Nano-Pearl-String" was obtained using electrospinning by Maier's group [42], indicating a universal growth mechanism associated with $TiNb_2O_7$ oxides. To determine the distribution of Ti, Nb and O elements in the titanium niobium binary oxide, elemental mappings of the representative pore structure unit were conducted in Fig. 3e-g, and the results matched well with high-angle annular dark-field scanning TEM (HAADF-STEM) image in Fig. 3d, revealing a homogeneous distribution of Ti, Nb and O atoms in 3DOM-$TiNb_2O_7$. The same conclusion can be further confirmed by the EDS result in Fig. S5.

Fig. 4a shows the nitrogen adsorption-desorption isotherms of 3DOM-$TiNb_2O_7$, and it presents a high Brunauer-Emmett-Teller (BET) surface area of 26.99 $m^2 g^{-1}$. The corresponding pore size distribution profile is shown in Fig. 4b along with the Barrett-Joyner-Halenda (BJH) pore diameter of 3DOM-$TiNb_2O_7$ based on adsorption curve, demonstration the presence of three different pore sizes. A pore diameters of 5.5 nm and 23 nm are caused by interparticle pores among the single-crystalline nanoparticles [43], and a broad pore size distribution from ~50 nm to ~130 nm, corresponding to the interconnecting pore obtained from the remove of adjacent PS microspheres, coinciding with a pore diameter of ~100 nm in Fig. 2c. As a whole, the obtained hierarchical porous structure is beneficial to the infiltration of electrolyte, and therefore enhances lithium ion transport kinetics [44].

In order to investigate the electrochemical performance of the 3DOM-$TiNb_2O_7$, half-cell lithium batteries were assembled and evaluated. Compared to single metal oxides, the $Li^+$ intercalation/deinter-

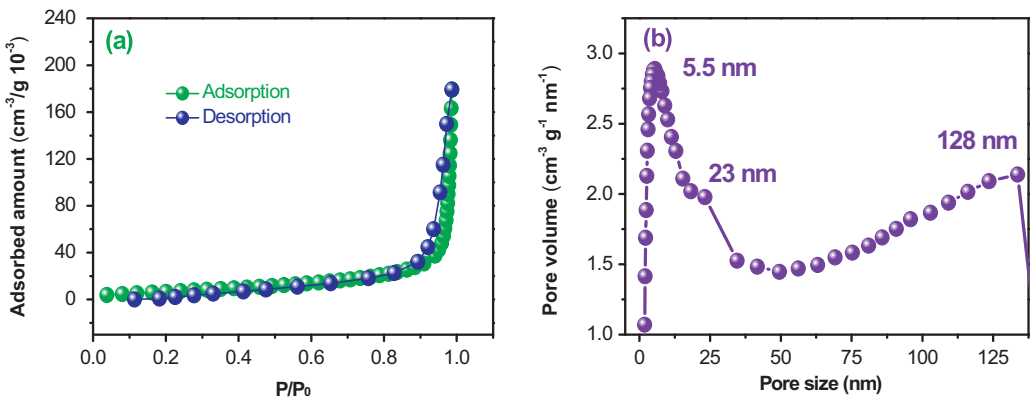


**Fig. 4.** (a) Nitrogen adsorption-desorption isotherm and (b) corresponding pore size distribution curve or 3DOM-$TiNb_2O_7$.

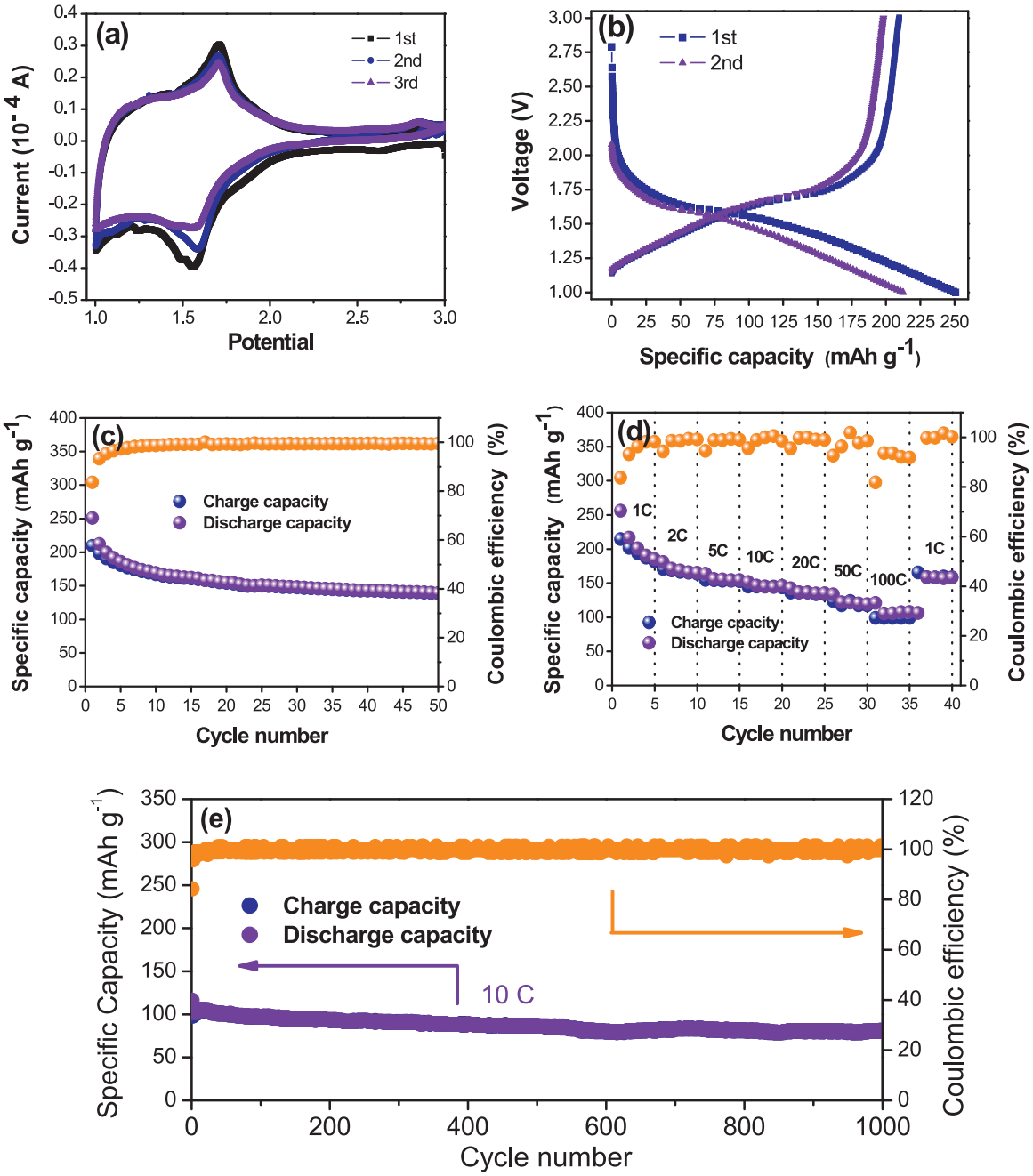


**Fig. 5.** (a) Cyclic voltammograms of the cell in the potential window of 1.0–3.0 V at a scan rate of 0.1 mV $s^{-1}$. (b) The initial two charge/discharge curves of $TiNb_2O_7$/Li half cell at 1 C; (c) Cycling performance and coulombic efficiency of the cell at 1 C, and (d) Rate capability of $TiNb_2O_7$ electrodes at various rate (1 C, 2 C, 5 C, 10 C, 20 C, 50 C, 100 C): discharge rate was fixed at 1 C. (e) Cycling performance and coulombic efficiency of $TiNb_2O_7$ anode at 10 C after 5 cycles at 0.1 C.

calation behavior of binary metal oxides is more complex due to synergistic effects occurring [45]. Herein, cyclic voltammetry was performed to study the electrochemical behavior of the 3DOM-$TiNb_2O_7$. As shown in Fig. 5a, the initial three cycles were carried out at a scan rate of 0.1 mV $s^{-1}$ between 1 and 3.0 V. A couple of obvious redox peaks can be observed at around 1.56 and 1.71 V, corresponding to the reduction/oxidation reaction of $Nb^{5+}/Nb^{4+}$ couple. Another couple of unconspicuous broad redox peaks can be seen at 1.81 and 1.90 V is attributed to the $Ti^{4+}/Ti^{3+}$ couple, and the broad bump in the range of 1.0–1.4 V can be assigned to the $Nb^{4+}/Nb^{3+}$ redox couple [20,23]. Notably, the phenomenon, reduction peak position in the first cycle differs from that in the subsequent cycles, is in virtue of the migration of the Fermi level and major distortion of the Nb (Ti)-oxygen octahedra during the insertion of lithium ions [13].

Fig. 5b shows the galvanic charge/discharge curves of the first two cycles in the range of 1–3.0 V at 1 C (387 mA $g^{-1}$). The initial two discharge and charge capacities are 251, 212 mA h $g^{-1}$ and 210, 198 mA h $g^{-1}$, corresponding to a coulombic efficiency of 84% and 93%, respectively. The reversible capacity deceases in the second cycle may be related to the channelling effects derived from distortion of the $MO_6$ (M=Ti, Nb) octahedra during charge/discharge process [13,46]. In addition, the discharge plateau, shown at approximately 1.65 V, ascribes to a two phase transformation process [16,47], and the two sloping regions (1.7–3.0 V and 1.0–1.5 V) are related to a solid-solution reaction [16]. The cycling performance of the 3DOM-$TiNb_2O_7$ at 1 C is presented in Fig. 5c. After 50 cycles the capacity of the cell reaches 139 mA h $g^{-1}$, corresponding to a capacity retention ratio of 65%. In order to study the fast lithium-ion transport and

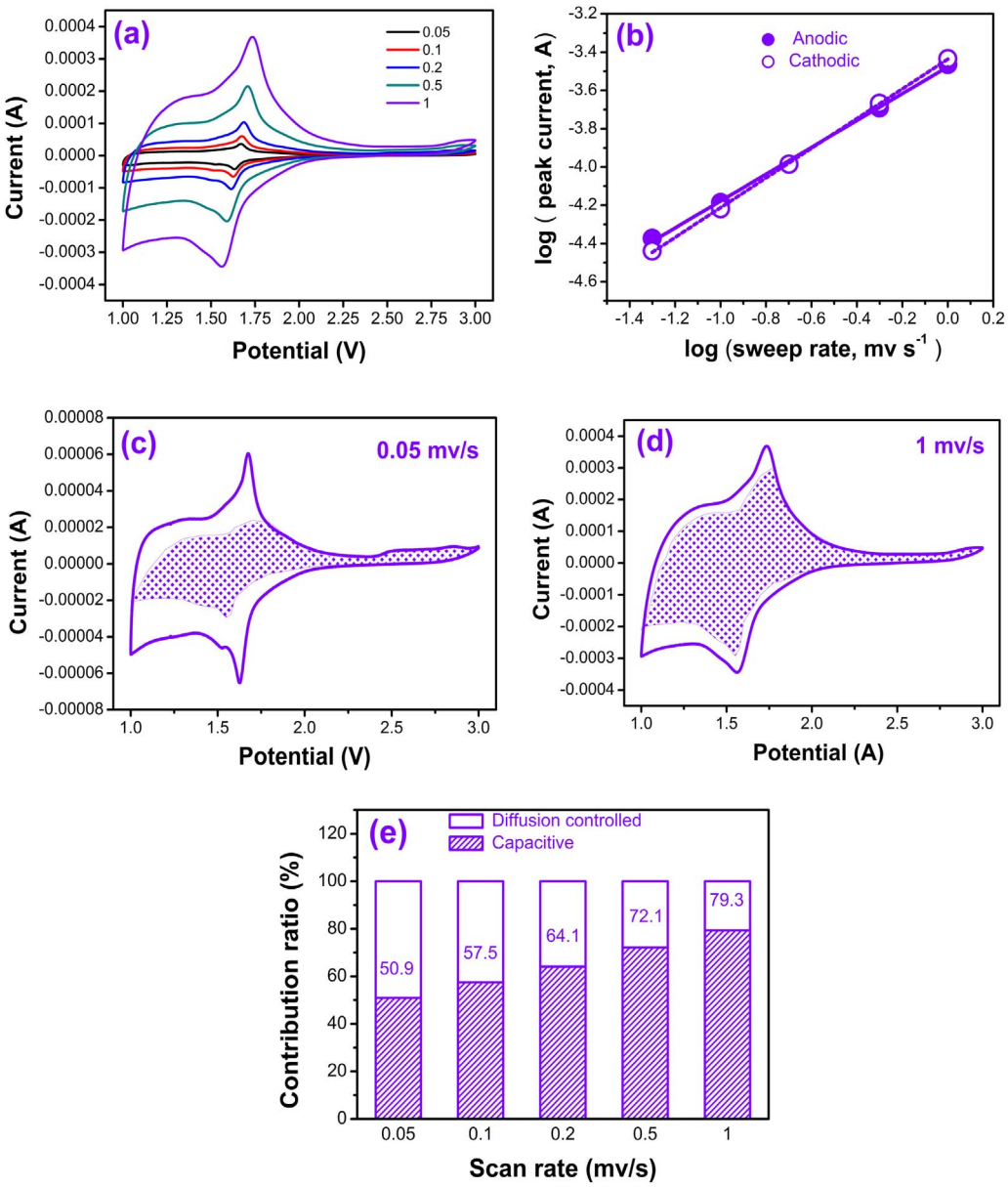


**Fig. 6.** (a) CV curves at various scan rates, from 0.05 to 1 mV $s^{-1}$. (b) Determination of the b-value using the relationship between peak current to sweep rate. (c, d) CV curves of 3DOM-$TiNb_2O_7$ with separation between total current (solid line) and capacitive currents (shaded regions) at (c) 0.05 mV $s^{-1}$ and (d) 1 mV $s^{-1}$. (e) Separation of contributions from capacitive and diffusion-controlled capacities at different sweep rates.

capacity recovery of $TiNb_2O_7$ electrodes, $TiNb_2O_7$/Li half cells were tested at various rates, ranging from 1 C to 20 C and then returned to 1 C (Fig. S6). The average charge capacity for 5 cycles are 206, 162, 124, 105 and 84 mA h $g^{-1}$ at a charge/discharge rate of 1 C, 2 C, 5 C, 10 C and 20 C respectively. Returning the rate back to 1 C results in the capacity recovering back to 184 mA h $g^{-1}$, indicating good electrochemical reversibility of the $TiNb_2O_7$ electrode. At the same time, it is worth noting that the mass-loading of electrodes is also a critical parameter except the value of specific capacity, and plays an important role in the battery design and configuring. High mass-loading can significantly improve the energy density of the full batteries within the limited space. Therefore, a lot of work devoted to improving the energy density through elevating the mass-loading of electrodes [48]. Typically, V. Aravindan and S. Madhavi et al. reported a high mass-loading of 5 mg $cm^{-1}$ for high energy density non-aqueous Li-ion capacitors using $TiO_2$-B nanorods and $TiO_2$ nanofibers [49,50], also observably promotion was achieved on the LIBs from their other work [51]. As a consequence, we believe that it is a meaningful research direction to enhance the mass loading of nanomaterials in the subsequent research on $TiNb_2O_7$ anodes.

Generally, EVs and HEVs will be charged at night in an effort to draw power at off-peak hours. On account of the sufficient time, the charge rate of the power lithium ion batteries can be decreased in order to increase the actual charge capacity. It worth to be noticed that the charging process of full batteries corresponds to $Li^+$ insertion into the anode material, therefore, the discharge rate of $TiNb_2O_7$/Li half cells can be reduced to investigate the real fast discharge performance of full battery pack. Herein, the discharge rate of $TiNb_2O_7$/Li half cell was fixed at 1 C while the charge rate was varied, as shown in Fig. 5d. Reversible capacities as high as 135 and 120 mA h $g^{-1}$ are achieved at charge rates of 20 C and 50 C, respectively. Even at an elevated charge rate of 100 C (38.7 A $g^{-1}$), a high capacity of 99 mA h $g^{-1}$ was obtained.

Fig. 5e shows the long-term cycling ability of 3DOM-$TiNb_2O_7$ electrodes at a charge/discharge rate of 10 C, following an activation process at 0.1 C. The capacity of the first and 1000th cycle are 106 and 87 mA h $g^{-1}$, respectively, reflecting a capacity retention of 82%. In

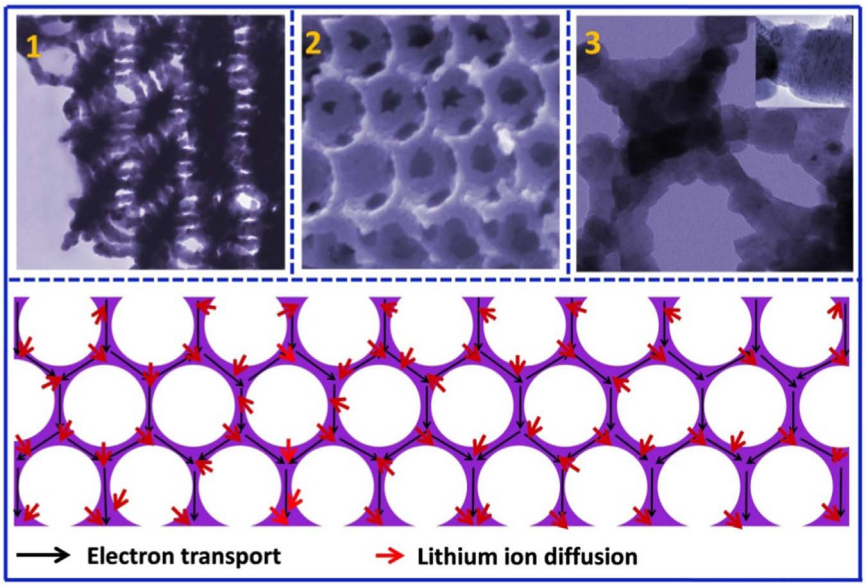


**Fig. 7.** Schematic illustration for the ion transport and electron transport in the 3DOM-$TiNb_2O_7$ anode materials, and the different structure characteristics of the 3DOM-$TiNb_2O_7$: 1) the sharp nanoscale interconnected walls, 2) two types of porosity, the macropores and the smaller quasi mesopores, 3) the rough surface and the single-crystallines nanoparticles.

addition, the coulombic efficiency was found to be nearly 100% in each cycle. The outstanding cycling performance can be attributed to the excellent structural integrity and crystallinity of the 3DOM-$TiNb_2O_7$ architecture.

Considering the large specific surface area and good rate capability of 3DOM- $TiNb_2O_7$, it can be theorized that electrochemical capacitance effects play a role in the fast charge/discharge process observed [52–54]. As well demonstrated, utilization of nanostructured materials as active electrodes can be beneficial for the improvement of high rate operations, for these arising reasons, 1) nanomaterials, especially the nanoparticles with dozens of nanometers, ensures most of the electrochemical reactions occurring on the surface and near-surface region of the electrodes, and thereby display typical pseudocapacitive $Li^+$ intercalation, in which the charge storage within the crystalline framework of these materials is not controlled by the $Li^+$ diffusion process [55]. 2) As the sizes of active materials decreasing to nanoscale, the crystalline structure would not undergo a phase transformation in Li+ intercalation process, leading to a high-effective enhancement of long-term cycle stability [56].

Herein, a quantitative analysis method [57,58] based on the cyclic voltammograms was used to further distinguish between capacitive and diffusion-limited contributions to the total observed capacity. Lithium-ion intercalation kinetics can be analyzed by plotting log($i$) versus log($v$) for anodic and cathodic peak currents. The measured current ($i$, A) obeys a power-law relationship with the sweep rate $v$ (mV $s^{-1}$) [59]:

$$i = av^b \tag{1}$$

where both $a$ and $b$ are adjustable parameters, with $b$-values derived from the slope of the plot of log $i$ vs log $v$. In particular, a $b$-value of 0.5 indicates a diffusion-controlled process caused by cations intercalation, while $b$=1 symbolizes a capacitive behavior via a surface faradaic redox reaction [27,60].

The CV curves at various scan rates from 0.05 to 1 mV $s^{-1}$ are shown in Fig. 6a, displaying similar shapes with broad peaks during both cathodic and anodic processes. It is interesting to note that the small peak separations are nearly identical when the scan rate is increased from 0.1 to 1 mV $s^{-1}$, demonstrating minimal polarization at high rates. To analyze the intrinsic electrochemical behavior, log($i$) versus log($v$) was plotted. As presented in Fig. 6b, the calculated b values are respectively 0.75 and 0.72 for cathodic and anodic current peaks, indicating that reaction current is derived from both lithium ion intercalation and surface capacitance. To distinguish quantitatively the capacitive contribution from the total current response through the voltammetric sweep rate, Eq. (1) is rewritten as [61].

$$i(\mathrm{V}) = k_1 v + k_2 v^{1/2} \tag{2}$$

where $k_1$ and $k_2$ are adjustable values. The total current, at a fixed potential $i$(V), is a combination of surface capacitive effects ($k_1 v$) and diffusion-controlled processes ($k_2 v^{1/2}$). For analytical purposes, Eq. (2) can be rearranged as follows:

$$i(\mathrm{V})/v^{1/2} = k_1 v^{1/2} + k_2 \tag{3}$$

By plotting $v^{1/2}$ versus $i/v^{1/2}$, $k_1$ and $k_2$ can be determined from the slope and the $y$-axis intercept point. Thus, based on the calculated $k_1$ and $k_2$, we are able to figure out the capacitive ($k_1 v$) and diffusion-limited ($k_2 v^{1/2}$) contributions at the specific fixed potentials. This analysis, outlined in Fig. 6c and d, where the shaded area ($k_1 v$, capacitive charge) and the experimental currents (solid line, total charge) are presented, and the diffusion-controlled charge is mainly generated at around the peak voltage. Based on this analysis, we determine that the total capacity of 3DOM-$TiNb_2O_7$ contributed by the capacitive effects increases with increasing scan rate. As sweeping rates increase from 0.05 to 1 mV $s^{-1}$, the proportion of surface capacitance-controlled capacity increase from 50.9% to 79.3%, as shown in Fig. 6e. The high contribution of capacitive charge storage in this case may be attributed to the large specific surface area derived from the 3DOM architecture composed of interconnected nano-crystallines, which provides sufficient active area for electrochemical $Li^+$ intercalation and de-intercalation, as well as cluster gaps or interstitial sites for lithium storage [62,63]. More importantly, the dominant capacitive charge storage mechanism enhances the high rate capability of 3DOM-$TiNb_2O_7$.

In view of the above results and analysis, the essential reasons of extraordinary high rate capability and excellent cycling performance can be summarized from three aspects, as illustrated in Fig. 7. Firstly, the nanoscale interconnected walls reduce polarization of the electrode. Due to the 3D ordered structure of the colloidal crystal template, 3DOM-$TiNb_2O_7$ exhibits porosity at two length scales: macropores, formed by the remove of PS spheres, and the smaller quasi mesopores, formed by contact points between PS spheres. This dual interconnected porous structure produces sharp nanoscale edges which are uniformly distribute throughout the electrode. Upon application of a potential, a

relatively high strength electric field develops at these sharp nanoscale edges, resulting in a weaker electric field in the remaining surface and reducing the overall polarization [28]. In addition, the 3DOM-$TiNb_2O_7$, with porous walls, display an open interconnected macroporous network and a nanoporous framework, which act as a reservoir/highway for electrolyte impregnation and ion transport [64]. Secondly, surface roughness improves lithium ion intercalation and deintercalation kinetics as defects allow for lithium ions to quickly intercalate into/de-intercalate from the electrode, minimizing sluggish solid-state ion transport [65,66]. Finally, nano-crystallites in the 3D architecture facilitate electron and ion transport during the charge/discharge process. Since the discharge process is a double injection procedure of ions and electrons [67,68], the electrical conductivity of $TiNb_2O_7$ anode will increase along with discharging, and therefore the electrochemical reaction rate is accelerated. Meanwhile, $Li^+$ diffusion lengths in the electrode material and electrolyte is reduced down to the nanometer scale, as a result, the resistances of both the electrode and the electrolyte decreases. From the above analysis, it can be concluded that the mechanism by which both electrons react and ions transport are three-dimensional nanoscale and, therefore, present obvious and highly-efficiency pseudocapacitive behavior. Due to that, favorable ion kinetics are achieved and the rapid $Li^+$ intercalation/de-intercalation are enhanced, leading to excellent rate capability and long-term cycle life at high rates.

## 4. Conclusion

In summary, we have successfully fabricated 3DOM-$TiNb_2O_7$ composed of interconnected single-crystallites using a self-assembly polystyrene (PS) microsphere template. When used as an anode material for lithium ion batteries, the obtained $TiNb_2O_7$, with a three-dimensional open macroporous and quasi mesopores structure, exhibit high rate performance and ultra-long cyclic stability. Reversible capacities as high as 135 and 120 mA h $g^{-1}$ were achieved at a charge rates of 20 C and 50 C, respectively. Even at elevated charge rates of 100 C (38.7 A $g^{-1}$), a capacity of 99 mA h $g^{-1}$ was obtained. Furthermore, a high capacity retention ratio of 82% can be achieved after 1000 cycles at 10 C with a maintained coulombic efficiency of nearly 100%. Such high electrochemical performance is attributed to the favorable kinetics resulting from the unique 3DOM architecture, which provides fast capacitive charge storage, leading to good rate capability and long-term cycle life. Our strategy of designing a 3DOM architecture of $TiNb_2O_7$ is a promising method for developing novel, high-power electrode materials. The results presented suggest that $TiNb_2O_7$ is a promising anode material for advanced lithium ion batteries for potential application in hybrid vehicles and pure electric vehicles.

## Acknowledgements

This work was supported by the National Natural Science Foundation of China (No. 51472065). G. Yin, Y. Ma and S. Lou would like to thank Dr. Yuyan Shao (PNNL) for discussion. S. L. and G. Y. would like to thank co-supervisor Prof. Xueliang (Andy) Sun for guidance and discussion. We also thank the financial support by Ph.D. Student Foreign Visiting Research Project Funding of Harbin Institute of Technology (HIT), and the academic support by the Nanomaterials and Energy Group of University of Western Ontario.

## Appendix A. Supporting information

Supplementary data associated with this article can be found in the online version at doi:10.1016/j.nanoen.2017.01.058.

## References

[1] J.M. Tarascon, M. Armand, Nature 414 (2001) 359–367.
[2] A.S. Arico, P. Bruce, B. Scrosati, J.-M. Tarascon, W. van Schalkwijk, Nat. Mater. 4 (2005) 366–377.
[3] V. Etacheri, R. Marom, R. Elazari, G. Salitra, D. Aurbach, Energy Environ. Sci. 4 (2011) 3243–3262.
[4] B. Scrosati, J. Hassoun, Y.-K. Sun, Energy Environ. Sci. 4 (2011) 3287–3295.
[5] G.-N. Zhu, H.-J. Liu, J.-H. Zhuang, C.-X. Wang, Y.-G. Wang, Y.-Y. Xia, Energy Environ. Sci. 4 (2011) 4016–4022.
[6] W. Chen, H. Jiang, Y. Hu, Y. Dai, C. Li, Chem. Commun. 50 (2014) 8856–8859.
[7] J.-T. Han, Y.-H. Huang, J.B. Goodenough, Chem. Mater. 23 (2011) 2027–2029.
[8] J.-T. Han, J.B. Goodenough, Chem. Mater. 23 (2011) 3404–3407.
[9] H. Li, L. Shen, J. Wang, S. Fang, Y. Zhang, H. Dou, X. Zhang, J. Mater. Chem. A 3 (2015) 16785–16790.
[10] S. Jayaraman, V. Aravindan, P. Suresh Kumar, W. Chui Ling, S. Ramakrishna, S. Madhavi, ACS Appl. Mater. Interfaces 6 (2014) 8660–8666.
[11] H. Park, H.B. Wu, T. Song, U. Paik, Adv. Energy Mater. (2015). http://dx.doi.org/10.1002/aenm.201401945.
[12] A.G. Ashish, P. Arunkumar, B. Babu, P. Manikandan, S. Sarang, M.M. Shaijumon, Electrochim. Acta 176 (2015) 285–292.
[13] X. Lu, Z. Jian, Z. Fang, L. Gu, Y.-S. Hu, W. Chen, Z. Wang, L. Chen, Energy Environ. Sci. 4 (2011) 2638–2644.
[14] G.N. Zhu, L. Chen, Y.G. Wang, C.X. Wang, R.C. Che, Y.Y. Xia, Adv. Funct. Mater. 23 (2013) 640–647.
[15] M.M. Thackeray, C. Wolverton, E.D. Isaacs, Energy Environ. Sci. 5 (2012) 7854–7863.
[16] B. Guo, X. Yu, X.-G. Sun, M. Chi, Z.-A. Qiao, J. Liu, Y.-S. Hu, X.-Q. Yang, J.B. Goodenough, S. Dai, Energy Environ. Sci. 7 (2014) 2220–2226.
[17] X. Wang, G. Shen, Nano Energy 15 (2015) 104–115.
[18] H. Song, Y.-T. Kim, Chem. Commun. 51 (2015) 9849–9852.
[19] C. Lin, S. Yu, S. Wu, S. Lin, Z.-Z. Zhu, J. Li, L. Lu, J. Mater. Chem. A 3 (2015) 8627–8635.
[20] L. Fei, Y. Xu, X. Wu, Y. Li, P. Xie, S. Deng, S. Smirnov, H. Luo, Nanoscale 5 (2013) 11102–11107.
[21] K. Tang, X. Mu, P.A. van Aken, Y. Yu, J. Maier, Adv. Energy Mater. 3 (2013) 49–53.
[22] C. Jo, Y. Kim, J. Hwang, J. Shim, J. Chun, J. Lee, Chem. Mater. 26 (2014) 3508–3514.
[23] H. Li, L. Shen, G. Pang, S. Fang, H. Luo, K. Yang, X. Zhang, Nanoscale 7 (2015) 619–624.
[24] H. Park, T. Song, U. Paik, J. Mater. Chem. A 3 (2015) 8590–8596.
[25] Z. Chen, V. Augustyn, X. Jia, Q. Xiao, B. Dunn, Y. Lu, ACS Nano 6 (2012) 4319–4327.
[26] V. Raju, J. Rains, C. Gates, W. Luo, X. Wang, W.F. Stickle, G.D. Stucky, X. Ji, Nano Lett. 14 (2014) 4119–4124.
[27] V. Augustyn, J. Come, M.A. Lowe, J.W. Kim, P.-L. Taberna, S.H. Tolbert, H.D. Abruña, P. Simon, B. Dunn, Nat. Mater. 12 (2013) 518–522.
[28] Z. Tong, J. Hao, K. Zhang, J. Zhao, B.-L. Su, Y. Li, J. Mater. Chem. C 2 (2014) 3651–3658.
[29] A. Blanco, E. Chomski, S. Grabtchak, M. Ibisate, S. John, S.W. Leonard, C. Lopez, F. Meseguer, H. Miguez, J.P. Mondia, G.A. Ozin, O. Toader, H.M. van Driel, Nature 405 (2000) 437–440.
[30] D. Li, M. Tian, R. Xie, Q. Li, X. Fan, L. Gou, P. Zhao, S. Ma, Y. Shi, H.-T.-H. Yong, Nanoscale 6 (2014) 3302–3308.
[31] D. Saritha, U. Varadaraju, Mater. Res. Bull. 48 (2013) 2702–2706.
[32] Q. An, Q. Wei, P. Zhang, J. Sheng, K.M. Hercule, F. Lv, Q. Wang, X. Wei, L. Mai, Small 11 (2015) 2654–2660.
[33] W. Cai, G. Lu, J. He, Y. Lan, Ceram. Int. 38 (2012) 3167–3174.
[34] L. Perfler, V. Kahlenberg, C. Wikete, D. Schmidmair, M. Tribus, R. Kaindl, Inorg. Chem. 54 (2015) 6836–6848.
[35] L. Liao, T. Fang, X. Zhou, Y. Gao, X. Cheng, L. Zhang, G. Yin, Solid State Ion. 254 (2014) 27–31.
[36] Z. Jian, X. Lu, Z. Fang, Y.-S. Hu, J. Zhou, W. Chen, L. Chen, Electrochem. Commun. 13 (2011) 1127–1130.
[37] Y. Luo, J. Luo, J. Jiang, W. Zhou, H. Yang, X. Qi, H. Zhang, H.J. Fan, D.Y.W. Yu, C.M. Li, T. Yu, Energy Environ. Sci. 5 (2012) 6559–6566.
[38] D.-l. Ma, Z.-y. Cao, H.-g. Wang, X.-l. Huang, L.-m. Wang, X.-b. Zhang, Energy Environ. Sci. 5 (2012) 8538–8542.
[39] J.-J. Xu, Z.-L. Wang, D. Xu, F.-Z. Meng, X.-B. Zhang, Energy Environ. Sci. 7 (2014) 2213–2219.
[40] S. Lou, Y. Ma, X. Cheng, J. Gao, Y. Gao, P. Zuo, C. Du, G. Yin, Chem. Commun. 51 (2015) 17293–17296.
[41] H. Zhang, Y. Wang, P. Liu, S.L. Chou, J.Z. Wang, H. Liu, G. Wang, H. Zhao, ACS Nano 10 (2016) 507–514.
[42] K. Tang, X. Mu, P.A. van Aken, Y. Yu, J. Maier, Adv. Energy Mater. 3 (2013) 49–53.
[43] M. Zhu, D. Meng, C. Wang, G. Diao, ACS Appl. Mater. Interfaces 5 (2013) 6030–6037.
[44] P.L. Taberna, S. Mitra, P. Poizot, P. Simon, J.M. Tarascon, Nat. Mater. 5 (2006) 567–573.
[45] F. Wu, J. Bai, J. Feng, S. Xiong, Nanoscale 7 (2015) 17211–17230.
[46] S. Lou, B. Shen, P. Zuo, G. Yin, L. Yang, Y. Ma, X. Cheng, C. Du, Y. Gao, RSC Adv. 5 (2015) 81235–81242.
[47] X. Wu, J. Miao, W. Han, Y.-S. Hu, D. Chen, J.-S. Lee, J. Kim, L. Chen, Electrochem. Commun. 25 (2012) 39–42.
[48] X. Li, M. Gu, S. Hu, R. Kennard, P. Yan, X. Chen, C. Wang, M.J. Sailor, J.-G. Zhang,

J. Liu, Nat. Commun. 5 (2014) 4105.
[49] V. Aravindan, N. Shubha, W.C. Ling, S. Madhavi, J. Mater. Chem. A 1 (2013) 6145–6151.
[50] V. Aravindan, J. Sundaramurthy, P.S. Kumar, N. Shubha, W.C. Ling, S. Ramakrishna, S. Madhavi, Nanoscale 5 (2013) 10636–10645.
[51] S. Jayaraman, V. Aravindan, N. Shubha, M. Ulaganathan, S. Madhavi, Part. Part. Syst. Charact. 33 (2016) 306–310.
[52] V. Aravindan, J. Gnanaraj, Y.-S. Lee, S. Madhavi, Chem. Rev. 114 (2014) 11619–11635.
[53] C. Chen, Y. Wen, X. Hu, X. Ji, M. Yan, L. Mai, P. Hu, B. Shan, Y. Huang, Nat. Commun. 6 (2015). http://dx.doi.org/10.1038/ncomms7929.
[54] R. Wang, J. Lang, P. Zhang, Z. Lin, X. Yan, Adv. Funct. Mater. 25 (2015) 2270–2278.
[55] P. Simon, Y. Gogotsi, B. Dunn, Science 343 (2014) 1210–1211.
[56] Y. Wang, Y. Song, Y. Xia, Chem. Soc. Rev. 45 (2016) 5925–5950.
[57] T. Brezesinski, J. Wang, J. Polleux, B. Dunn, S.H. Tolbert, J. Am. Chem. Soc. 131 (2009) 1802–1809.
[58] V. Augustyn, P. Simon, B. Dunn, Energy Environ. Sci. 7 (2014) 1597–1614.
[59] H. Lindström, S. Södergren, A. Solbrand, H. Rensmo, J. Hjelm, A. Hagfeldt, S.-E. Lindquist, J. Phys. Chem. B 101 (1997) 7717–7722.
[60] E. Lim, H. Kim, C. Jo, J. Chun, K. Ku, S. Kim, H.I. Lee, I.-S. Nam, S. Yoon, K. Kang, J. Lee, ACS Nano 8 (2014) 8968–8978.
[61] J. Wang, J. Polleux, J. Lim, B. Dunn, J. Phys. Chem. C 111 (2007) 14925–14931.
[62] K. Zhao, F. Liu, C. Niu, W. Xu, Y. Dong, L. Zhang, S. Xie, M. Yan, Q. Wei, D. Zhao, L. Mai, Adv. Sci. 2 (2015). http://dx.doi.org/10.1002/advs.201500154.
[63] O.B. Chae, J. Kim, I. Park, H. Jeong, J.H. Ku, J.H. Ryu, K. Kang, S.M. Oh, Chem. Mater. 26 (2014) 5874–5881.
[64] L. Xia, S. Wang, G. Liu, L. Ding, D. Li, H. Wang, S. Qiao, Small 12 (2016) 853–859.
[65] D. Su, A. McDonagh, S.-Z. Qiao, G. Wang, Adv. Mater. (2016). http://dx.doi.org/10.1002/adma.201604007.
[66] S. Chen, G. Liu, H. Yadegari, H. Wang, S.Z. Qiao, J. Mater. Chem. A 3 (2015) 2559–2563.
[67] Z. Tong, H. Xu, G. Liu, J. Zhao, Y. Li, Electrochem. Commun. 69 (2016) 46–49.
[68] H. Li, H. Zhou, Chem. Commun. 48 (2012) 1201–1217.

**Shuaifeng Lou** is currently a Ph.D. candidate under the supervision of Prof. Geping Yin in Harbin Institute of Technology (HIT), China. At the same time, he is a visiting student at Prof. Xueliang (Andy) Sun's Nanomaterials and Energy Group, University of Western Ontario, Canada. He received his B. E. at Harbin Engineering University in 2010, and then joined Prof. Geping Yin's group at HIT and got his M. E. in 2012. His current research interest focus on oxides anode materials for high-power LIBs and $Li^+$ hybrid cpacitors.

**Xinqun Cheng** is currently an Associate Professor at School of Chemistry and Chemical Engineering, Harbin Institute of Technology (HIT), China. He received his Ph.D. at HIT in 2005. He has published the book of "Electrochemical Power Sources", which has been widely used for textbook in higher-education colleges. He has taken charge of several research programs funded by National Natural Science Fund, Ministry of Education, etc. His research interest focus on new electrochemical power sources, including electrode materials for lithium ion battery and aluminum-air battery et al.

**Yang Zhao** is currently a Ph.D. candidate in Prof. Xueliang (Andy) Sun's Nanomaterials and Energy Group at the University of Western Ontario, Canada. He received his B.S. degree and M.S. degree in Chemical Engineering and Technology from Northwestern Polytechnical University (Xi'an, China) in 2011 and 2014, respectively. His current research interests focus on atomic layer deposition in the application of lithium/sodium ion batteries and all solid state batteries.

**Andrew Lushington** is currently a Ph.D. candidate in prof. Xueliang (Any) Sun's Nanomaterials and Energy Group at the University of western Ontario. He received his B.Sc in Chemistry with a Concentration in Nanotechnology and a minor in Religion from Carleton University (Ottawa, Canada) in 2012. His current research interest is predominantly in the area of atomic and molecular layer deposition for the application and use in energy storage and energy conversion devices.

**Jinlong Gao** is currently a Ph.D. candidate in Harbin Institute of Technology (HIT), China. He received his B. E. and M. E. at HIT in 2013 and 2015, respectively. Now, it is his second year as Ph.D. student. His research interest focus on materials for electrochemical energy storage, including anode for lithium ion battery, lithium ion hybrid capacitors and sodium ion battery.

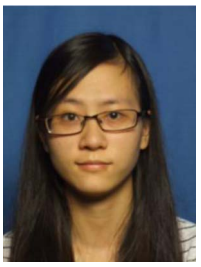

**Qin Li** is currently a Ph.D. student at Harbin Institute of Technology supervised by Prof. Yunzhi Gao. She received her Bachelor degree and Master degree from Harbin Institute of Technology, China, in 2012 and 2014, respectively. Her main research interests include electrode materials for lithium-ion batteries, inorganic solid electrolyte and all-solid-state Li-ion batteries.

**Pengjian Zuo** is currently a Professor in Chemistry and Chemical Engineering at Harbin Institute of Technology (HIT). He received the B. E. and Ph.D. degree in Chemical Engineering and Technology at HIT in 2002 and 2007, respectively. He was a visiting scholar at Jiguang (Jason) Zhang's Group, Pacific Northwest National Laboratory in 2012–2013. His current research interests focus on high-performance cathode materials for LIBs and Li-S batteries.

**Biqiong Wang** is currently a Ph.D. candidate in Prof. Xueliang (Andy) Sun's Nanomaterials and Energy Group at the University of Western Ontario, Canada. She received her Bachelor degree in Materials Science in 2012 at the City University of Hong Kong. Her research interests are associated with the application of atomic layer deposition in all-solid-state batteries. She is also co-supervised by Prof. T. K. Sham from Chemistry Department in the University of Western Ontario. Part of her work is related to the study of energy materials via synchrotron radiation.

**Yunzhi Gao** is currently a Professor in School of Chemistry and Chemical Engineering at Harbin Institute of Technology, China. He received his B. E. at HIT in 1982, and then received his Ph.D. degree at Hokkaido University, Japan, in 1994. He worked at Riken Corporation as a research fellow before he came back to work in China. In 2010, he was introduced to Harbin Institute of Technology as overseas talents. Dr. Gao's research interest lies in electrochemical power source, full cell and in-situ electrochemical analysis technique.

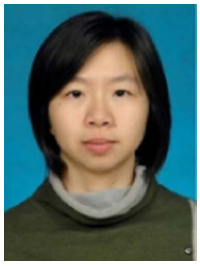

**Yulin Ma** is currently an Associate Professor in Chemistry and Chemical Engineering at Harbin Institute of Technology (HIT), China. She got the Ph.D. degree in Chemical Engineering and Technology at HIT in 2010. She was a visiting scholar at Lawrence Berkeley National Laboratory in 2014-2015. Her current research interests focus on high-performance Li-rich cathode materials for LIBs.

**Chunyu Du** is a Professor in School of Chemistry and Chemical Engineering at Harbin Institute of Technology (HIT), China. He received his B. E., M. E. and Ph.D. degree at HIT in 1998, 2000 and 2004, respectively. He was a postdoctoral fellow at Hong Kong University of Science and Technology in 2006–2007. His current research interests are associated with high-performance ternary (NCA, NCM), Li-rich cathode materials for LIBs and advanced electrocatalysis in PEMFCs.

**Geping Yin** is a Full Professor in School of Chemistry and Chemical Engineering at Harbin Institute of Technology (HIT), China. She got the B. E. in Electrochemical Engineering at HIT in 1982. Then she stayed at HIT as a teacher up to now, and received her Ph.D. degree at HIT in 2000. She has gone to Yokohama National University (2008) as a visiting scholar. She continuously entered the list of the Elsevier Most Cited Chinese Researchers in 2015 and 2016. Her current research interests focus on the fields of advanced electrochemical catalysis process for PEMFC, advanced electrode materials for LIBs and other chemical power sources systems et al.

**Xueliang (Andy) Sun** is a Full Professor and a Canada Research Chair at the University of Western Ontario, Canada. Dr. Sun received his Ph.D. in Materials Chemistry under direction of Prof. George Thompson in 1999 at the University of Manchester, UK, followed by work as a postdoctoral fellow under direction of Prof. Keith Mitchell at the University of British Columbia, Canada, and as a Research Associate under direction of Prof. Jean-Pol Dodelet at l'Institut national de la recherché scientifique (INRS), Canada. His current research interests are associated with synthesis of low-dimensional nanomaterials for electrochemical energy storage and conversion. His research focus is on design and synthesis of various one-dimensional nanostructures such as nanotubes, nanowires, nanoparticles and nanofilms as well as their composites as electrocatalysis and catalyst support in fuel cells and as anode and cathodes in lithium ion batteries and Li–air batteries.